Influence of wave-front curvature on supercontinuum energy during filamentation of femtosecond laser pulses in water

F. V. Potemkin,[1,*] E. I. Mareev,[1] and E. O. Smetanina[2,3]

[1]*Faculty of Physics and International Laser Center, M. V. Lomonosov Moscow State University, Moscow 119991, Russia*

[2]*Université Bordeaux, Centre National de la Recherche Scientifique, CEA, Centre Lasers Intenses et Applications, UMR 5107, 33405 Talence, France*

[3]*Department of Physics, University of Gothenburg, SE-412 96 Göteborg, Sweden*

(Received 29 October 2017; revised manuscript received 2 February 2018; published 1 March 2018)

We demonstrate that using spatially divergent incident femtosecond 1240-nm laser pulses in water leads to an efficient supercontinuum generation in filaments. Optimal conditions were found when the focal plane is placed 100–400 μm before the water surface. Under sufficiently weak focusing conditions [numerical aperture (NA) < 0.2] and low-energy laser pulses, the supercontinuum energy generated in divergent beams is higher than the supercontinuum energy generated in convergent beams. Analysis by means of the unidirectional pulse propagation equation shows a dramatic difference between filamentation scenarios of divergent and convergent beams, that explains corresponding features of the supercontinuum generation. Under strong focusing conditions (NA ≥ 0.2) and high-energy laser pulses, the supercontinuum generation is suppressed for convergent beams in contrast to divergent beams that nevertheless are shown experimentally to allow supercontinuum generation. The presented technique of the supercontinuum generation in divergent beams in water is highly demanded in a development of femtosecond optical parametric amplifiers.

DOI: 10.1103/PhysRevA.97.033801

I. INTRODUCTION

Femtosecond laser filamentation has attracted the interest of the scientific community since the development of ultrashort-pulse high-power laser sources. Outstanding technologies such as microwave antennas, weather control, distance energy transport, and terahertz and laser sources in the atmosphere are based on laser filaments. From the fundamental point of view, laser-pulse filamentation is a unique physical system to study the laser-matter interaction due to the various involved mechanisms. Laser-pulse filamentation results from the dynamic balance between linear and nonlinear material and self-induced plasma responses to the strong electric field of the incident laser beam. The nonlinear processes, Kerr self-focusing, and plasma defocusing enrich the frequency-angular spectrum of the pulse leading to the generation of a supercontinuum (SC) and a conical emission (CE) [1–7]. The decrease of the pulse duration caused by these nonlinear processes can reach a few-cycle scale that, in condensed matter, increases the influence of the chromatic dispersion on the pulse propagation. Depending on the sign of the group velocity dispersion, the pulse can be split into subpulses or is localized in space and comoving time as a quasisoliton [8–10]. If the pulse intensity reaches the optical breakdown threshold, a material damage can be observed along the filament trace [11]. An external focusing condition is applied to control a filament length from kilometer to subcentimeter scale. However, aberrations can affect the pulse intensity distribution and increase the threshold for the most nonlinear optical processes [12]. Depending on the focusing conditions, a transition from linear to nonlinear filamentation regime can be observed [13,14]. While a long-scale filamentation is promising for light detection and ranging (LIDAR) technologies, a short-scale-filamentation and SC generation in bulk media is highly demanded for a wide range of applications such as ultrafast subcycle high-resolution spectroscopy and as a seeder for optical parametric amplifiers [15–17].

The goal of this paper is to evaluate conditions for an efficient SC generation by focused femtosecond laser pulses in water. Both experimentally and numerically, we investigate two cases of laser-pulse focusing geometry: a water sample is placed after or before the focal plane of the beam, thus the incident laser beam has a divergent or convergent spatial phase correspondingly. We vary the laser-pulse energy, focus position, and numerical aperture (NA) to find out the most favorable conditions for an efficient SC generation. We report that the most efficient energy conversion to the SC is achieved in the case of a divergent laser beam.

The paper is organized as follows. In Secs. II and III we describe our experimental technique for the measurement of the SC energy in the visible spectral region, and present the SC energy map in coordinates of incident laser-pulse energy and of position of the water sample and the beam focal plane for NA equal to 0.05 and 0.1, respectively. We show the conditions when the energy of the visible SC is higher for divergent beam filamentation compared with the convergent beam filamentation. The corresponding SC spectra generated by both divergent and convergent beams are presented. In Sec. IV, numerical modeling by means of the unidirectional pulse propagation equation is employed to investigate the differences in the filamentation regimes for divergent and convergent laser pulses. The comparison of the experimentally

*potemkin@physics.msu.ru

measured and numerically obtained SC spectra generated by incident laser pulses with divergent and convergent spatial phases is followed by Sec. V, presenting the SC stability measurements and conclusion on the possible applications of the observed SC generation features.

II. EXPERIMENTAL SETUP

A Cr:forsterite laser system was used with the following parameters: $\lambda_0 = 1240$ nm, $\tau_{\mathrm{FWHM}} \approx 200$ fs, laser energy up to 2 mJ with fluctuations less than 5%, intensity contrast about 5×10^9 ASE, and repetition rate of 10 Hz. The laser-pulse energy was varied by a half wave plate and a Glan prism. The Ge detector (Thorlabs PDA50-B) measured the incoming laser energy. An iris was used for spatial filtering of the incoming laser beam and, being optimized once, afterwards it was not changed during all experiments. The laser beam was focused into the water cell (at open water-air boundary) by lenses and objectives with different NAs in the range 0.03–0.5 that leads to filamentation accompanied by a bright SC and CE. When using condensed dielectric samples (YAG, heavy water, fused silica, LiF, CaF_2), the position of the sample was varied to avoid the impact of the accumulated (during one measurement) structural changes on the following measurements. A scanning slit photodetector was used to record photoemission from plasma channels along the filament.

The SC and CE were collimated by an off-axis parabola and coupled into the spectrometer [for the visible wing, Solar SL40-2-3648USB; for the near infrared (IR) region, Solar SDH IV] or into a Si photodetector (PDA-100A) to measure the combined SC and CE energy in the visible range E_{SC}. The accumulation time for the spectra was set to 7 μs. The following procedure was employed to join the SC spectrum measurements performed in the visible and near-IR spectral ranges.

(1) The visible part of the SC (250–1050 nm) was measured by the spectrometer Solar SL40-2-3648USB and the IR part (900–1400 nm) was measured by the spectrometer Solar SDH-IV.

(2) The spectrum in the overlapping region (900–1050 nm) was additionally acquired by the monochromator equipped with a germanium photodetector. Using this data the conversion factor for both spectrometers was determined.

(3) Using the conversion factor the two spectra from the visible and near-IR part were joined.

(4) Finally, the joined SC spectrum was normalized on its maximum.

The 20-mm water cell was mounted onto the stepper motor in order to vary its input surface position with respect to the focal plane. The energy of the visible SC, E_{SC}, and corresponding spectra were measured for various incident laser energies E and distances Δz_f between the air-water interface z_{in} and the beam focal plane z_{FP}: $\Delta z_f = z_{\mathrm{FP}} - z_{\mathrm{in}}$. In case 1 (C1), the focal plane is located before the air-water interface ($\Delta z_f < 0$) and the incident pulse has a divergent wave front when interacting with water. In case 2 (C2), the focal plane is placed after the air-water interface ($\Delta z_f > 0$) and the incident pulse has a convergent wave front.

III. ENERGY MAPS OF THE VISIBLE SUPERCONTINUUM

For sufficiently low NA (0.05 and 0.1) the energy of the SC in the visible spectral range has been measured for various incident-pulse energies $E = 5$–$450\ \mu$J and water cell positions $\Delta z_f \in [-500, 1000]\ \mu$m [Figs. 1(a)–1(d)]. When the laser pulse is focused onto the water surface in a 10-μm spot with peak intensity $I_0 \gtrsim 10^{13}$ W cm^{-2} the high electron plasma density ($n_e \approx 10^{22}$ cm^{-3}) is reached and a plasma mirror is created [18]. It starts to deflect the incoming laser pulse and significantly distorts the central and tail laser-pulse time slices. In this regime, the SC generation is not efficient and a wide drop in the vicinity of $\Delta z_f = 0$ is observed [Figs. 1(a)–1(d)].

The stronger the focusing (the larger the NA) or the higher the energy of the incident pulse, the deeper the "drop" in the SC-generation map induced by the plasma mirror, that is governed by the incident pulse intensity at the water surface [18]. Thus, the plasma mirror leads to a two-area structure in each map. When using the water sample, the E_{SC} in C2 is larger for the lower NA [Figs. 1(c) and 1(d) black lines]. This observation is in agreement with previously reported decrease of E_{SC} with decrease of the focal length of the objective [13]. However, at low incident pulse energies $E < 100\ \mu$J, the energy of the SC generated by the pulse with divergent spatial phase $E_{\mathrm{SC}}^{(1)}$ is higher than the SC energy generated by

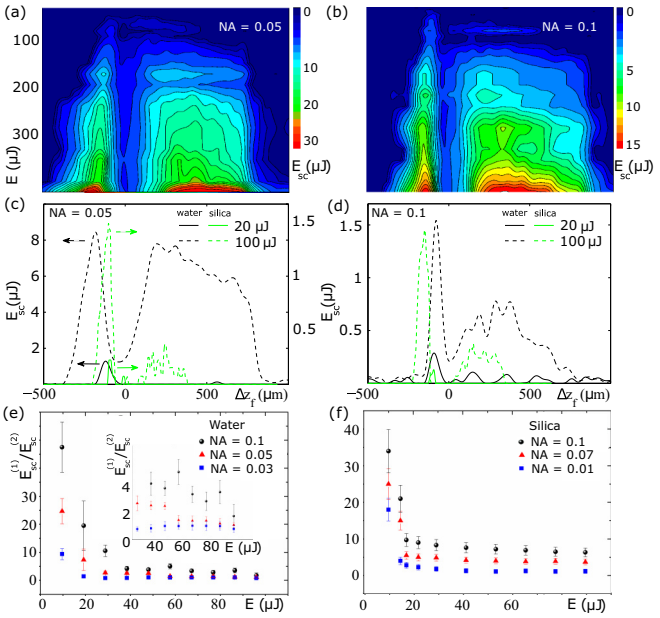

FIG. 1. Map of the SC energy $E_{\mathrm{SC}}(\Delta z_f, E)$ generated under filamentation in water (a, b) with corresponding profiles $E_{\mathrm{SC}}(\Delta z_f)$ at fixed laser-pulse energies E (c, d): (a, c) NA = 0.05; (b, d) NA = 0.1. (c, d) Solid and dashed lines correspond to $E = 20$ and 100 μJ, respectively; black and green (light gray) lines correspond to water and fused silica samples, respectively. (c) The SC energy values are presented on the left axis for water and on the right axis for fused silica. The ratio $E_{\mathrm{SC}}^{(1)}/E_{\mathrm{SC}}^{(2)}$ for various incoming laser energies E and focusing NA is presented in (e) and (f) for water and fused silica samples correspondingly. (e, f, h) The position of the water sample was characterized by $|\Delta z_f| \approx 200$–$300\ \mu$m, that corresponds to the most efficient SC generation in both C1 and C2.

the pulse with convergent spatial phase $E_{SC}^{(2)}$ [Figs. 1(c) and 1(d) black lines]. At higher energies ($E > 100\,\mu$J) the SC generation efficiency tends to be the same for divergent and convergent beams.

We observe the same regime of efficient SC generation in C1 compared to C2 in the materials YAG, heavy water, fused silica, LiF, and CaF_2, that allows us to report on the generality of the observed SC generation features in a divergent beam in dielectrics with similar electronic properties. The profiles $E_{SC}(\Delta z_f)$ generated in a fused silica sample at fixed laser-pulse energies 20 and 100 μJ are presented by green (light gray) lines in Figs. 1(c) and 1(d). Nevertheless, our method of SC generation in a divergent beam in water has a strong advantage over the alternative technique in glass plates, because filamentation in liquids allows us to work with extremely high intensities without irreversible damage of the material and to reach higher SC generation efficiency in a particular range of the incident pulse energies. Thus, in the following we concentrate on the SC generation in the water sample.

The regime of an efficient SC generation by the divergent laser pulse is obtained for a narrow range of sample positions relative to the focal plane of the incident beam, $\Delta z_f \in [-400,-100]\,\mu$m, while a less efficient SC generation regime by the convergent laser pulse can be realized in a wide range of focal positions $\Delta z_f \in [100,1000]\,\mu$m. To show the practical importance of the SC generation in C1 we compare the ratios between the energy in the visible part of the SC in C1 and C2, $E_{SC}^{(1)}/E_{SC}^{(2)}$, measured for incident laser-pulse energy range $E = 10$–$100\,\mu$J and various focusing NAs in water [Fig. 1(e)]. Additionally the $E_{SC}^{(1)}/E_{SC}^{(2)}$ measured for the SC generation in the fused silica sample is presented to illustrate the dependence of $E_{SC}^{(1)}/E_{SC}^{(2)}$ on the laser-pulse energy E that is similar to the one obtained for the water sample [Fig. 1(f)]. SC generation in C1 is much greater than in C2 for higher NA and lower pulse energies E (E close to the threshold needed for Kerr nonlinearity to overcome the diffraction and plasma absorption and defocusing in C1). Indeed, at incident pulse energy $E = 10\,\mu$J the ratio $E_{SC}^{(1)}/E_{SC}^{(2)}$ is 40 for NA = 0.1, and it drops down under 20 for the lowest considered NA both for water and for fused silica samples. For energies $E > 40\mu$J, $E_{SC}^{(1)}/E_{SC}^{(2)}$ is already less than 10 for all considered NAs and materials. The absolute value of the generated E_{SC} increases with the incident laser-pulse energy in the considered range. E_{SC} is higher for lower NA when using the water sample, and E_{SC} does not change significantly with varying NA from 0.05 to 0.1 when using the fused silica sample [Figs. 1(c)–1(f)].

The SC spectra $S(\lambda)$ generated by a 100-μm laser pulse in the water sample in C1 and C2 at NA = 0.1 were measured to show the distribution of the energy in the visible SC [Fig. 2(a)]. The region of spectral components in the blue wing of the SC that were collected for the visible SC energy measurements discussed in Secs. II and III is indicated by the violet-color area in Fig. 2(a).

The SC spectrum varies with the focusing parameter Δz_f that illustrates the observed features of the SC energy maps [Figs. 1(b) and 1(d)]. The SC generation is suppressed due to the plasma mirror when the sample surface is in the focal plane of the incident beam $\Delta z_f = 0$ [Fig. 2(a) black line] and the

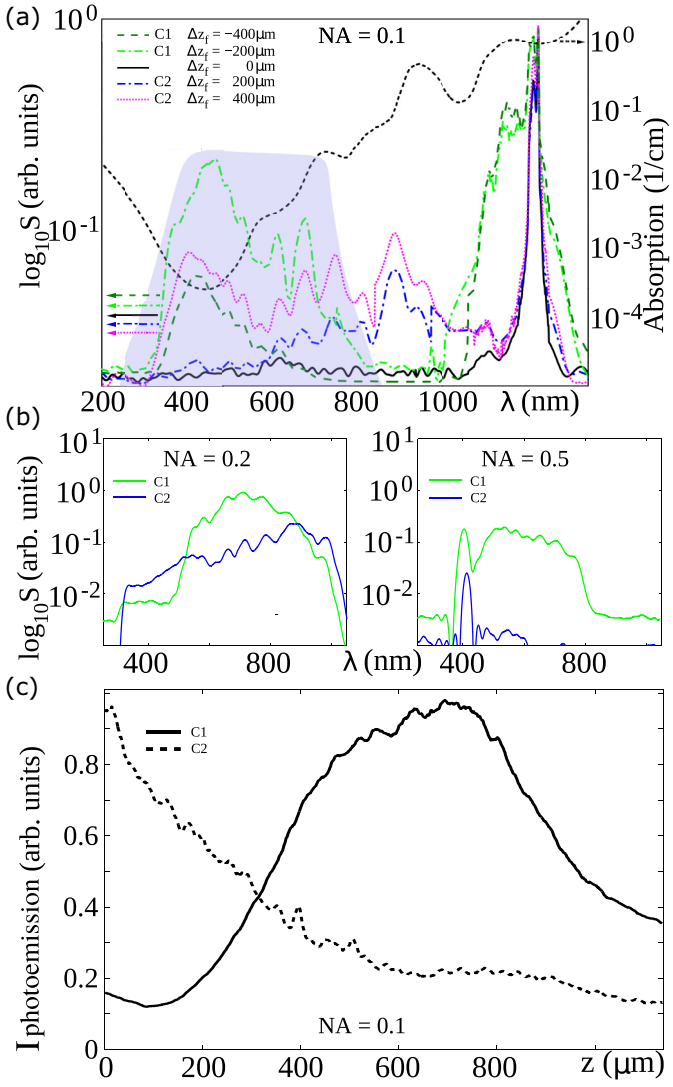

FIG. 2. (a) The experimentally detected SC spectra in logarithmic scale $\log_{10}S(\lambda)$ under filamentation of a 100-μJ laser pulse in water for various $|\Delta z_f|$ are presented together with the water absorption (black dotted line) in the considered spectral range. C1 is presented by light green (light gray) dash-dotted and dark green (black) dashed lines; C2 is presented by blue (black) dash-dotted and rose (light gray) dotted lines. The corresponding $|\Delta z_f|$ is indicated in the figure. The violet (light gray) area illustrates the visible spectral region for which the SC energy measurements were done. (b, c) The blue part of the SC spectra $S(\lambda)$ under strong focusing conditions. The NA is indicated in the figure. The spectral peak at 413 nm in (c) is related to the third-harmonic generation. Green (light gray) and blue (black) lines correspond to C1 and C2, respectively. (d) A typical photoemission of plasma channels $I_{\text{photoemission}}$ is presented for C1 and C2, NA = 0.1 and $E \approx 70$–$100\,\mu$J. $I_{\text{photoemission}}$ is normalized to its maximum, that is 0.52 and 0.11 a.u. in C1 and C2, respectively. The position of the water sample is characterized by $|\Delta z_f| \approx 200$–$300\,\mu$m, that corresponds to the most efficient SC generation in both C1 and C2. The laser-pulse energy is $E = 100\,\mu$J.

measured energy of the visible part of the SC E_{SC} is zero. In C1 ($\Delta z_f < 0$), the highest amplitudes of the spectral components in the visible frequency range are reached at $\Delta z_f = -200\,\mu$m [Fig. 2(a) green (light gray) dash-dotted line]. Corresponding

to the SC energy map (Fig. 1), the amplitudes of the visible part of the SC spectrum decrease when Δz_f goes from -200 to $-400\,\mu$m [Fig. 2(a) dark green (black) dashed line]. In C2 ($\Delta z_f > 0$), the visible part of the SC is not developed at $\Delta z_f = 200\,\mu$m [Fig. 2(a) blue (black) dash-dotted line], and the spectral amplitudes reach higher values at $\Delta z_f = 400\,\mu$m [Fig. 2(a) rose (light gray) dotted line]. The maximal reached SC amplitudes are higher in C1 than in C2, that corresponds to the measured SC energy ratio $E_{\rm SC}^{(1)}/E_{\rm SC}^{(2)} \approx 2$ [Fig. 1(e)].

The water absorption weakly affects the spectral region from 300 to 500 nm [Fig. 2(a) dotted black line], where the most intense blue wing SC components are developed. The SC components at longer wavelengths are strongly absorbed in water, resulting in a nonlinear-enhanced linear absorption of SC components during the filamentation process leading to additional laser-pulse energy losses.

For sufficiently high NA (0.2 and 0.5) the blue part of the SC spectra $S(\lambda)$ was measured experimentally in C1 and C2 at incident laser-pulse energy $E = 100\,\mu$J [Fig. 2(b)]. With an increase of the NA, the efficiency of the SC generation in both cases decreases. Within the strong-focusing conditions (NA > 0.2), the SC is generated only in C1. In C2 the SC generation is suppressed.

To investigate the spatial distribution of the SC sources, i.e., the high-intensity areas along the filament, a plasma-channel photoemission for C1 and C2 was detected [Fig. 2(c)]. Both in C1 and C2 the plasma channels start from the surface of the water sample and its emission decays with increase of z. Moving further inside the water sample along z, in C1 a new plasma growth appears at $z \approx 2$ mm indicating that the contribution of Kerr self-focusing is stronger than plasma defocusing and diffraction, while in C2 the plasma photoemission continues to decrease with z without formation of following plasma channels. Thus, no refocusing occurs in C2.

IV. NUMERICAL SIMULATIONS: PULSE EVOLUTION SCENARIOS

The simulations are performed using the GUPPECORE program packet [19,20] both in two-dimensional (2D)+1 and three-dimensional (3D+1 geometries. The 1240-nm laser pulse (Gaussian in space and time) with diameter $a =$ 3–4.1 mm, duration $\tau_{\rm FWHM} = 200$–350 fs, and peak intensities 1–2 $\times 10^8$ W cm^{-2} is focused by a 60-mm lens on the air-water interface. The parameters of the simulation are as follows: the multiphoton ionization cross-section is 3.6×10^{-146} m^{18} W^{-9} s^{-1}, the characteristic time of impact ionization is 1 fs [21,22], the band gap is taken at 8 eV, the linear refractive index at 1240 nm is $n = 1.32$, the nonlinear refractive index is $n_2 = 3 \times 10^{-20}$ m^2 W^{-1}, and the corresponding critical power for self-focusing is $P_{\rm cr} = 5.8$ MW. Considering 3D+1 geometry we introduce intensity fluctuations in the beam profile. The fluctuations have a Gaussian spatial form with spatial correlation parameter equal to $10\,\mu$m and amplitude parameter $a_{\rm fluct}$ is varied from 0 to 0.5. The fluctuation density is taken at $6 \times 10^{-2}\,\mu$m^{-2}. Numerically obtained scenarios of pulse spatiotemporal evolutions in C1 and C2 shed light on the experimentally detected features of the generated SC.

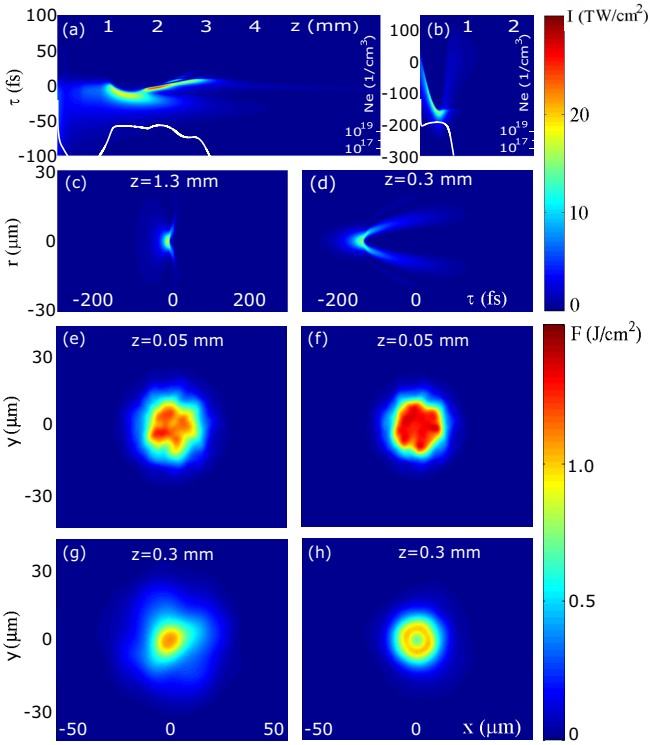

FIG. 3. 2D+1 modeling: Intensity evolution $I(r = 0,\tau,z)$ and plasma density $N_e(r = 0,z)$ along z for a 200-fs 7-μJ ($5.6P_{\rm cr}$, $a_{\rm FWHM} = 4.1$ mm) laser pulse (a) in C1, $\Delta z_f = -270\,\mu$m, and (b) in C2, $\Delta z_f = 300\,\mu$m; spatiotemporal intensity distribution $I(\mathrm{r},\tau)$ is shown at the propagation distances (c) in C1, 1.3 μm, and (b) in C2, 0.3 μm. 3D+1 modeling: Evolution of fluence $F(x,y)$ along the filament trace in water (g, h) in C1, $\Delta z_f = -300\,\mu$m, and (i, j) in C2, $\Delta z_f = 300\,\mu$m. $a_{\rm fluct} = 0.5$, $\tau_{\rm FWHM} = 330$ fs, $E = 7\,\mu$J, $P = 5P_{\rm cr}$, $a = 3$ mm.

Numerical scenarios of spatiotemporal evolution of the low-energy ($P < 10P_{\rm cr}$) laser pulse under sufficiently weak focusing conditions (NA $= 0.05$) in C1 and C2 are simulated in 2D+1 geometry (radial symmetry). The scenarios are characterized by the evolution of the on-axis pulse intensity distribution $I(r = 0,\tau,z)$ along the propagation distance z [Figs. 3(a) and 3(b)]. In C1 the nonlinear focus is reached at $z = 1$ mm and the maximum intensity of 2.4×10^{13} W cm^{-2} is achieved during refocusing cycles leading to a strong spectral broadening as will be shown later [Fig. 3(a)]. For longer pulse duration (330 fs), the number of the refocusing cycles increases and they occur in different time slices of the pulse tail (not shown here). In C2 the maximum intensity is only 1.7×10^{13} W cm^{-2} and no refocusing cycles occur [Fig. 3(b)]. For longer pulse duration (330 fs) also no refocusing cycles were found. Due to the interplay between focusing geometry, self-focusing, plasma defocusing, and absorption, in C1 plasma defocusing influences only the pulse tail while the central time slices of the pulse are still compressed in space [Fig. 3(c)], and the peak plasma density N_e is not higher than 6×10^{19} cm^{-3}. In contrast, the central time slices are defocused together with the pulse tail in C2 [Fig. 3(d)] and the peak plasma density reaches a slightly higher value $N_e = 1 \times 10^{20}$ cm^{-3}. This strong plasma defocusing in C2 prevents the following refocusing cycles and thus prevents the SC generation. For

sufficiently long laser pulses considered here, in C2 the electron avalanche is well developed due to a strong flux of laser-pulse intensity from the periphery to the center of the beam caused by strong focusing geometry, while in C1 the electron avalanche is less developed due to lower intensity flux from the periphery to the center of the beam caused by a competition between Kerr nonlinearity on one hand and diffraction and plasma defocusing on the other hand. In C2 when varying Δz_f from 250 to 600 μm, the only change is the position of the focus. In C1 when going from $\Delta z_f = -250$ to $-330\,\mu$m the distance to the nonlinear focus increases and the number of refocusing cycles decreases. No filament is formed for $|\Delta z_f| \geqslant 335\,\mu$m for the considered laser-pulse energy in C1. We do not consider the focal position that is closer than 250 μm to the water surface in numerical simulations because of the strong backward reflection at the surface plasma mirror, that cannot be modeled by UPPE simulations. Thus, the experimentally obtained higher bound of $|\Delta z_f|$ for filamentation in C1 is confirmed numerically. Thus, no refocusing cycles were found in C2, that is in good agreement with experimental observations of corresponding plasma channel emission.

The presented scenarios are sufficiently stable in 3D+1 geometry with perturbations introduced in the beam profile, that is demonstrated by the evolution of the pulse fluence spatial distribution $F(x,y)$ along the propagation distance z. In C1 [Fig. 3(e)] the filament is formed from an intensity fluctuation, that is located about 1–3 μm from the beam center ($x = 0, y = 0$), or in the center of the beam if there is no perturbation introduced in the input beam profile. At $z = 0.3$ mm, $F(x,y)$ has only one hot point close to the on-axis region [Fig. 3(g)], that corresponds to a surviving filament. In C2 the geometrical focusing governs the evolution of the laser pulse [1] [Figs. 3(f) and 3(h)]. The filament is formed strictly on-axis both in presence and in absence of the beam profile perturbations. $F(x,y)$ at the propagation distance $z = 0.3$ mm shows the formation of the ring structure that is caused by the strong defocusing of the laser pulse and losses on plasma absorption [23] in the self-induced laser plasma [Fig. 3(h)]. Thus, the two scenarios similar to those obtained in 2D+1 geometry are found also in 3D+1 geometry with introduced perturbations, that allows us to apply the main conclusions for the radial-symmetry case to the experimental conditions.

Next, the numerically obtained SC spectra in C1 and C2 are compared with the experimentally detected blue part of SC and the central part of the SC spectra. The weak anomalous group velocity dispersion (GVD) at 1240 nm in water allows us to generate a widely broadened spectrum in the anti-Stocks spectral region with a narrow dip separating the blue wing of the spectrum from its central part [4,24]. Such a dip between the central part of the spectrum around $\lambda_0 = 1240$ nm and the blue part of the SC may appear due to the destructive interference of the SC components [25] during the pulse propagation and was observed also in silica glass, YAG, and fluorides [5,26–28]. Alternatively, the blue peak formation can be explained in terms of high-order dispersion affecting the x-wave formation in the filamentation process [29,30].

In C1, the numerically simulated blue wing of the SC decreases and its maximum component shifts to the red while changing Δz_f from -270 to $-330\,\mu$m [Fig. 4(a) solid, dashed, and dash-dotted green (light gray) lines]. This decrease of

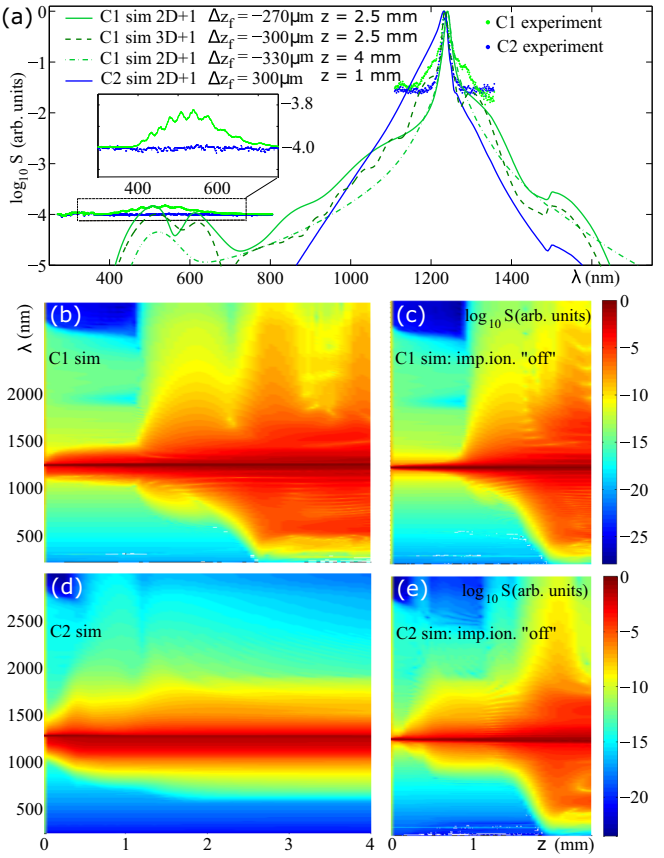

FIG. 4. (a) Numerical (lines) and experimental (dots) SC spectra in logarithmic scale $\log_{10} S(\lambda)$. The maximal amplitude of the experimentally detected blue wing of the SC is normalized to be equal to the maximal amplitude of the blue wing of the numerically calculated spectra for $\Delta z_f = -270\,\mu$m [solid green (light gray) line]. Pulse parameters in the simulations for both 2D+1 and 3D+1 geometries: $\tau_{\mathrm{FWHM}} = 200$ fs, $E = 7\,\mu$J ($5.6 P_{\mathrm{cr}}$), $a = 4.1$ mm. The fluctuation amplitude in 3D+1 is $a_{\mathrm{fluct}} = 0.5$. In the experiment $E = 35\,\mu$J. Propagation distances z at which $\log_{10} S(\lambda)$ were taken are indicated in the figure. (b–e) Numerically obtained evolution of the angularly integrated SC spectrum along the laser-pulse propagation distance z. C1 ($\Delta z_f = -300\,\mu$m) and C2 ($\Delta z_f = 300\,\mu$m) are presented in (b, c) and (d, e), respectively. (b, d) The modeling includes all the process as described in Sec. IV. (b) The impact ionization term is switched off, i.e., it is removed from the plasma density ionization rate equation in the simulation. The pulse parameters are $\tau_{\mathrm{FWHM}} = 330$ fs, $E = 7\,\mu$J, $P = 5 P_{\mathrm{cr}}$, $a = 3$ mm.

the visible SC component amplitude with increase of $|\Delta z_f|$ corresponds to the experimentally observed decrease of E_{SC} with increase of $|\Delta z_f|$ in C1 [Fig. 1(c)]. The spectral position of the numerically obtained blue wing [Fig. 4(a) green (light gray) lines] coincides with the experimentally observed spectrum of the visible SC [Fig. 4(a) green (light gray) dots]. In C2 the simulated SC broadening does not reach the visible spectral range [Fig. 4(a) blue (black) line], that confirms the experimentally detected absence (with respect to the noise level) of the blue wing of the SC [see inset in Fig. 4(a) blue (black) dots]. In our particular case of 1240-nm laser-pulse filamentation in water, the SC generation around the central wavelength and the generation of the red wing of the SC

are strongly suppressed by the neighboring wide absorption region corresponding to the first overtone of the H_20 molecule. This absorption mechanism is not included in the numerical model, that explains the differences between the numerical and experimental SC spectra around the central wavelength $\lambda_0 = 1240$ nm.

In C1, the spectrum superbroadening occurs during the pulse refocusing cycles where sufficiently high peak intensity can be reached [Fig. 3(a)]. In contrast, in C2 no refocusing cycles occur [Fig. 3(b)] and the highest reached intensity is not sufficient for an effective SC generation. To illustrate the impact of the electron avalanche in the laser-pulse evolution scenario and the SC generation in C1 and C2, we perform simulations with an artificial condition: the impact ionization term is removed from the ionization rate equation. In C1, a slightly shorter propagation distance for spectrum superbroadening can be reached in the simulation when the impact ionization term is removed from simulation [Figs. 4(b) and 4(c)]. The main features of SC generation and particularly the wide blue wing of the SC are kept without changes by switching off the impact ionization term in C1. In C2, the absence of the impact ionization term leads to a dramatic change of the pulse spectrum evolution [Figs. 4(d) and 4(e)] due to the appearance of the refocusing cycles in the filament. In C2 the SC generation is suppressed when the impact ionization term is included and, in contrast, the SC generation is developed in C2 as well as in C1 when the impact ionization term is removed from the simulation. Thus, the impact ionization is responsible for such a difference between C1 and C2: by artificial switching off of the impact ionization term in simulation, the refocusing cycles in which the peak intensity reaches sufficiently high values appear in both C1 and C2, and the difference in SC generation between these regimes vanishes [Figs. 4(c)–4(e)].

Note that the difference between the laser-pulse energies considered numerically ($7\,\mu$J) and experimentally ($35\,\mu$J) is due to the absence of the losses on (1) the linear water absorption and (2) the backward reflection in the UPPE simulations.

(1) The linear absorption decreases the laser-pulse energy that was injected in the water sample on 10% after 1-mm propagation distance when working at 1240-nm central wavelength. Thus, when accounting for the linear absorption in the simulations, the incident laser-pulse energy that is required for an appearance of the refocusing cycles in the filament and corresponding SC generation increases. The linear absorption will also affect the SC spectrum in the region above 600 nm [Fig. 2(a) black dotted line] during the filamentation process. As we are focused on the blue wing of the SC spectrum, we are confident that the considered features of the laser-pulse spectrum evolution in both C1 and C2 are adequately reproduced by the presented modeling.

(2) The backward reflection of the laser pulse occurs due to formation of a surface $1/10$-μm-thick layer of laser-induced plasma during the laser-dielectric surface interaction process [31]. A backward-reflected laser-pulse fluence grows, while the transmitted fluence stays under the damage threshold with an increase of the incident laser-pulse fluence over the damage threshold [31]. For pulse duration $\tau_{\mathrm{FWHM}} \approx 200$ fs considered in this paper, the critical fluence needed for the critical plasma density creation on the sample surface is about $4\,\mathrm{J/cm^2}$ (corresponding to the pulse energy $E = 12.6\,\mu$J) and the estimated transmitted fluence is about $2\,\mathrm{J/cm^2}$ ($E = 6.3\,\mu$J) [31]. Thus, in our simulations, we take the incident laser-pulse energy $E = 7\,\mu$J that is close to the estimated transmitted value ($6.3\,\mu$J) to reproduce the evolution of the part of the laser pulse that was injected in the water sample and undergoes the filamentation process accompanied by SC generation.

V. STABILITY OF THE SUPERCONTINUUM

The discovered experimental regime of the efficient SC generation by divergent beam (C1) may be potentially used as a seeder for femtosecond optical parametric amplifiers. For seeding applications the rms noise value of the SC energy is particularly important since it impacts the final laser stability [32]. Our SC stability measurements show that the SC generation is more stable in C1 than in C2. In water, at incident laser-pulse energy $E = 100\,\mu$J, the rms noise of the energy in the visible part of the SC in C1 is 5%, and in C2 it is 7%. The rms noise of the spectral amplitudes in the range from 300 to 450 nm is 5.6 and 8% in C1 and C2, respectively. The rms noise of the SC spectral amplitudes decreases for the spectral range 450–600 nm: it is 4.7% in C1 and 6.6% in C2. The rms noise increases for larger wavelengths: it is 5.1% in C1 and 7.2% in C2 from 600 to 750 nm, and it is 5.2% in C1 and 7.9% in C2 from 750 to 850 nm. The SC stability in C1 is close to the stability of the pump laser, that is 5%. The rms noise below 2% is preferable for various applications [32–35]. When using the SC as a seed, the stability of the idler wave can be higher than the stability of the SC seed [35], that may allow to use the divergent beam SC with 5% rms as a seed for optical parametric amplifiers.

VI. CONCLUSION

In conclusion, we experimentally and numerically studied two regimes of femtosecond filamentation in water. These regimes differ by the water sample position relative to the focal plane: the water sample is placed after the focal plane (C1) and the water sample is located before the focal plane (C2). In C1 we found a narrow range of focal positions before the water surface that provide an efficient SC generation. The plasma channel in C1 is longer and the electron density in this channel is lower than in C2. In C1 the energy is efficiently transformed into the SC, that propagates along the optical axis. The difference between C1 and C2 manifests more clearly under tighter focusing conditions and lower laser-pulse energies. If NA > 0.2, there is no SC generation at higher energies in C2, while C1 still provides the SC generation under these conditions.

ACKNOWLEDGMENTS

The authors acknowledge the high-performance computing resources of TGCC under GENCI Allocation No. A0010506129 and funding by Russian Science Foundation Grant No. 17-72-20130. Spectral measurements were partially supported by Russian Foundation for Basic Research Grant No. 17-02-01065 and FASIE Grant No. 10528GU2/2016. Guillaume Duchateau is acknowledged for fruitful discussions.

[1] S. Skupin and L. Berge, Opt. Commun. **280**, 173 (2007).
[2] A. Couairon and A. Mysyrowicz, Phys. Rep. **441**, 47 (2007).
[3] J. Bethge, A. Husakou, F. Mitschke, F. Noack, U. Griebner, G. Steinmeyer, and J. Herrmann, Opt. Express **18**, 6230 (2010).
[4] P. Vasa, J. A. Dharmadhikari, A. K. Dharmadhikari, R. Sharma, M. Singh, and D. Mathur, Phys. Rev. A **89**, 043834 (2014).
[5] N. Garejev, G. Tamošauskas, and A. Dubietis, J. Opt. Soc. Am. B **34**, 88 (2017).
[6] J. Jiang, Y. Zhong, Y. Zheng, Z. Zeng, X. Ge, and R. Li, Phys. Lett. A **379**, 1929 (2015).
[7] F. V. Potemkin, E. I. Mareev, A. A. Podshivalov, and V. M. Gordienko, New J. Phys. **117**, 53010 (2015).
[8] L. Bergé and S. Skupin, Phys. Rev. E **71**, 065601 (2005).
[9] A. Couairon, E. Gaižauskas, D. Faccio, A. Dubietis, and P. Di Trapani, Phys. Rev. E **73**, 016608 (2006).
[10] P. P. Kiran, S. Bagchi, C. L. Arnold, S. R. Krishnan, G. R. Kumar, and A. Couairon, Opt. Express **18**, 21504 (2010).
[11] A. Couairon, L. Sudrie, M. Franco, B. Prade, and A. Mysyrowicz, Phys. Rev. B **71**, 125435 (2005).
[12] A. A. Dergachev, A. A. Ionin, V. P. Kandidov, D. V. Mokrousova, L. V. Seleznev, D. V. Sinitsyn, E. S. Sunchugasheva, S. A. Shlenov, and A. P. Shustikova, Quantum. Electron. **44**, 1085 (2014).
[13] W. Liu, O. Kosareva, I. Golubtsov, A. Iwasaki, A. Becker, V. Kandidov, and S. Chin, Appl. Phys. B **76**, 215 (2003).
[14] K. Lim, M. Durand, M. Baudelet, and M. Richardson, Sci. Rep. **4**, 7217 (2014).
[15] D. Kartashov, S. Ališauskas, A. Pugžlys, A. Voronin, A. Zheltikov, M. Petrarca, P. Béjot, J. Kasparian, J.-P. Wolf, and A. Baltuška, Opt. Lett. **38**, 3194 (2013).
[16] J. Kasparian and J.-P. Wolf, Opt. Express **16**, 466 (2008).
[17] H. Liang, P. Krogen, R. Grynko, O. Novak, C.-L. Chang, G. J. Stein, D. Weerawarne, B. Shim, F. X. Kärtner, and K.-H. Hong, Opt. Lett. **40**, 1069 (2015).
[18] W. Tibor, Complete characterization of plasma mirrors and development of a single-shot carrier-envelope phase meter, Ph.D. thesis, University of Szeged, 2010, http://doktori.bibl.u-szeged.hu/id/eprint/1568.
[19] J. Andreasen and M. Kolesik, Phys. Rev. E **86**, 036706 (2012).
[20] M. Kolesik and J. V. Moloney, Phys. Rev. E **70**, 036604 (2004).
[21] J. Noack and A. Vogel, IEEE J. Quantum Electron. **35**, 1156 (1999).
[22] C. Sarpe-Tudoran, A. Assion, M. Wollenhaupt, M. Winter, and T. Baumert, Appl. Phys. Lett. **88**, 261109 (2006).
[23] S. Skupin, R. Nuter, and L. Bergé, Phys. Rev. A **74**, 043813 (2006).
[24] J. A. Dharmadhikari, R. A. Deshpande, A. Nath, K. Dota, D. Mathur, and A. K. Dharmadhikari, Appl. Phys. B **117**, 471 (2014).
[25] A. E. Dormidonov and V. P. Kandidov, Laser Physics **19**, 1993 (2009).
[26] E. O. Smetanina, V. O. Kompanets, S. V. Chekalin, A. E. Dormidonov, and V. P. Kandidov, Opt. Lett. **38**, 16 (2013).
[27] M. Durand, K. Lim, V. Jukna, E. McKee, M. Baudelet, A. Houard, M. Richardson, A. Mysyrowicz, and A. Couairon, Phys. Rev. A **87**, 043820 (2013).
[28] A. Dormidonov, V. Kompanets, S. Chekalin, and V. Kandidov, Opt. Express **23**, 29202 (2015).
[29] D. Faccio, A. Averchi, A. Lotti, M. Kolesik, J. V. Moloney, A. Couairon, and P. Di Trapani, Phys. Rev. A **78**, 033825 (2008).
[30] D. Faccio, A. Averchi, A. Couairon, A. Dubietis, R. Piskarskas, A. Matijosius, F. Bragheri, M. A. Porras, A. Piskarskas, and P. Di Trapani, Phys. Rev. E **74**, 047603 (2006).
[31] M. Feit, A. Komashko, and A. Rubenchik, Appl. Phys. A **79**, 1657 (2004).
[32] A. van de Walle, M. Hanna, F. Guichard, Y. Zaouter, A. Thai, N. Forget, and P. Georges, Opt. Lett. **40**, 673 (2015).
[33] M. Bradler, P. Baum, and E. Riedle, Appl. Phys. B **97**, 561 (2009).
[34] U. Megerle, I. Pugliesi, C. Schriever, C. F. Sailer, and E. Riedle, Appl. Phys. B **96**, 215 (2009).
[35] P. Rigaud, A. V. de Walle, M. Hanna, N. Forget, F. Guichard, Y. Zaouter, K. Guesmi, F. Druon, and P. Georges, Opt. Express **24**, 26494 (2016).